Letter

Tunable visible comb using Raman self-frequency shift, intermodal phase matching and cascading of nonlinearities in an all-fiber platform

Akhileshwar Mishra, Seth Mathew V, and Ravi Pant*

Laboratory of Phoxonics and Nonlinear Optics in Nanostructures (PHONON), School of Physics, Indian Institute of Science Education and Research (IISER), Thiruvananthapuram, Kerala 695551, India

(Received 4 May 2022; accepted 29 March 2023; published 1 May 2023)

Up-conversion of IR frequency combs from compact erbium fiber mode-locked lasers (MLLs) around 1550 nm is enabling the development of small-footprint visible combs for ultralow-power spectroscopy and quantum optics. Limited tunability of the IR MLLs, due to the small gain bandwidth (∼30 nm) of erbium fiber amplifiers, and difficulty in achieving broadband phase matching for up-conversion in a nonlinear crystal or waveguide restricts the visible comb wavelengths to second- and third-harmonic wavelengths. Here, we harness the soliton self-frequency shift (SSFS) of sub-nJ energy mode-locked IR pulses in a standard single-mode silica fiber and combine it with the up-conversion, through cascading of optical nonlinearities, in a dispersion-engineered silica nanowire to achieve wideband tuning of the second-, third-, fourth-, and sixth-harmonic generated (SHG, THG, FHG, SiHG) signals. By varying the fiber length and the IR pump power, we Raman shift the pump wavelength from 1560 to ∼1750 nm using the SSFS and use it to tune the wavelengths of the THG and SHG signals in a 10-mm-long silica nanowire from 520 to 578 nm and 780 to ∼850 nm, respectively. Four-wave mixing between the THG and SHG signals creates a tunable signal close to the fourth-harmonic (390 nm), and SHG of THG creates a tunable SiHG in the deep UV (260 nm). The generation and tuning of deep UV (∼260 nm) to near-IR combs (∼780 nm) using redshifted IR solitons demonstrate that the cascading of optical nonlinearities in a silica nanowire enables spectral translation between wavelength regimes that are more than five octaves apart.

DOI: 10.1103/PhysRevResearch.5.L022020

Small-footprint visible comb sources will benefit applications, e.g., photon-level spectroscopy, quantum interference, and astrocombs [1–8]. Creating a microresonator Kerr comb in the visible region is challenging due to the normal dispersion of most of the optical materials in the visible wavelength region [9–11]. The translation of IR combs from compact mode-locked lasers (MLLs) in the 1550 nm wavelength region, which can be implemented on-chip as well [12], through harmonic generation in nonlinear crystals and waveguides has been used to create compact visible combs [1,3,6,13]. The frequency of the up-converted signal in all these demonstrations is, however, fixed at the harmonic of the MLL frequency due to the lack of broadband phase matching and limited wavelength tuning range of the MLLs, which severely restricts the application of the visible comb to only systems operating at the harmonic frequency. However, many applications require visible combs in different wavelength regions, which can be achieved by using different setups and devices [1,2].

The soliton self-frequency shift (SSFS) of mode-locked pulses has long been used to create widely tunable ultrashort pulse sources by redshifting the input soliton wavelength in tapered and photonic crystal fibers (PCFs) [14–22]. In many of these demonstrations, high peak power pulses from large-footprint Ti:sapphire MLLs are used to achieve wideband redshift [23]. Blueshift of near-IR (NIR) wavelength (∼800 nm) pulses from these MLLs, through second- and third-harmonic generation (SHG, THG) in nonlinear crystal and waveguides [24], has been driving the development of visible sources for applications in frequency metrology [25], UV spectroscopy [26], astrocombs [7], and RNA detection [27]. However, frequency tuning of the blueshifted sources, in general, is limited due to the challenges in achieving broadband phase matching in up-converting devices and limited wavelength tunability of the MLLs. Further, many of the nonlinear crystals and waveguides support either second- or third-order nonlinearity, which further restricts the wavelength range of the up-converted signals. A simple way to realize a widely tunable visible comb is to first create a widely tunable pulse source through redshifting of the input pulses and then blueshift these pulses in a medium with broadband phase matching. In [28], the SSFS of mode-locked pulses, centered at 1240 nm, from a Cr:forsterite laser was used to redshift the solitons to 1600 nm in a PCF. The up-converison of the redshifted soliton in the PCF was then used to create a third-harmonic signal around ∼530 nm. However, tuning of the THG signal was not demonstrated in these experiments due to the lack of broadband phase matching. In these experiments, 80 fs, 100 nJ energy mode-locked pulses from a

*rpant@iisertvm.ac.in

Cr:forsterite laser amplifier system were used to achieve peak powers of ∼100 kW.

Here we report the simultaneous generation and wideband tuning of the four-harmonic components, namely, second-, third-, fourth- and sixth-harmonic generation (SHG, THG, FHG, SiHG), in a single silica nanowire. We exploit the Raman-induced self-frequency shift of the sub-nJ energy mode-locked IR (1560 nm) pulses in a single-mode fiber (SMF) to tune the MLL frequency, and use the broadband phase matching and cascading of optical nonlinearities in a silica nanowire to simultaneously achieve SHG, THG, FHG, and SiHG of the redshifted pulses for creating a widely tunable visible comb in an all-fiber platform. While the centrosymmetric nature of silica prohibits the existence of even-order nonlinearity, SHG has been predicted and observed in silica nanowires due to surface-induced nonlinearities and multipole contributions [29,30]. Earlier SHG, THG, and SiHG have been achieved in silica nanowires with efficiencies of 10^{-7}, 10^{-5}, and 10^{-3}, respectively [13]. However, in these demonstrations, the frequency of the harmonics was restricted by the MLL frequency. By propagating the IR pulses through different SMF lengths, we tune their wavelength from 1560 to 1750 nm. Using the harmonic generation of these Raman-shifted IR pulses in a 10-mm-long silica nanowire, we achieve a large tuning of the THG signal from 520 to 578 nm (∼66 THz) and SHG signal from 780 to 850 nm (∼34 THz). For a fixed SMF length, we tune the wavelength of the Raman-shifted pulses by varying the pulse energy and use it to demonstrate pump-power-dependent tuning of all the harmonic components. We tune the FHG signal wavelength from 370 to 415 nm (∼88 THz) and SiHG signal from 260 to 300 nm (∼170 THz). A silica nanowire provides a versatile platform as it not only enables a tunable comb across multiple visible regions, but also allows enhanced light-matter interaction through the trapping of atoms [31–34]. Pump-power-controlled wavelength tuning of the IR, SHG, THG, FHG, and SiHG in an all-fiber platform, using a single source, therefore, opens different avenues in visible comb spectroscopy [1] and quantum optics [3].

Figures 1(a)–1(c) show a schematic of the processes, namely, (a) soliton self-frequency shift (SSFS), (b) intermodal phase matching, and (c) cascading of optical nonlinearities, involved in the creation of a tunable visible comb across four different visible spectral windows. Figure 1(a) shows the intrapulse Raman-scattering-mediated SSFS of an ultrashort pulse on propagation through a standard SMF, which has anomalous group-velocity dispersion β_2 in the wavelength region around 1550 nm. For efficient SSFS, a significant part of the input pulse spectrum redshifts to new frequency ω_s. Complete transfer of the pump signal to the redshifted signal is, however, difficult to achieve due to the variation in the value of the group-velocity dispersion (β_2) and nonlinearity parameter (γ) as the pump redshifts (see Eq. (2) in the Supplemental Material [35]) [36]. For large redshifts, a decrease in the SSFS efficiency reduces the power of the redshifted soliton. The energy band at ω_s [inset of Fig. 1(a)] represents the frequency tuning of the Raman Stokes photon, which can be achieved by varying the pulse width and power, and SMF length (see Eqs. (1) and (2) in the Supplemental Material [35]). SSFS only redshifts the IR pump wavelength, whereas visible comb generation requires a blueshift of the pump wavelength. The creation of a tunable IR source through SSFS alone, therefore, does not guarantee a tunable visible comb.

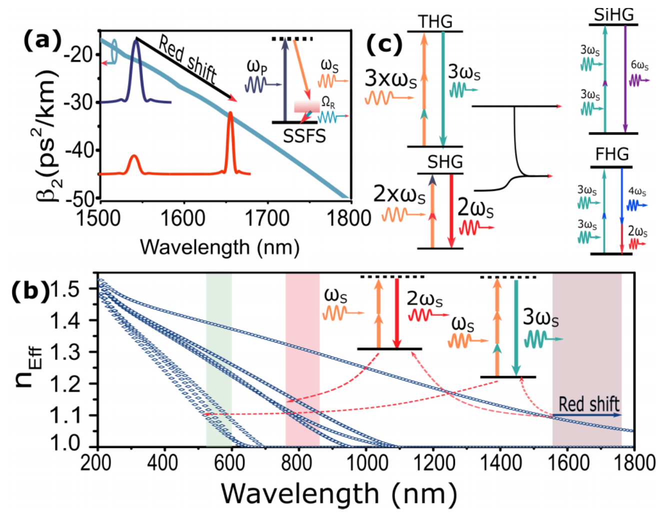

FIG. 1. Concept of tunable visible comb using SSFS and cascaded optical nonlinearities. (a) The GVD parameter of SMF and concept of the SSFS-induced redshift of the pulse spectrum. (b) Modal dispersion of the tapered fiber showing phase matching of the higher-order modes at the THG and SHG wavelengths with the pump mode. (c) Pathways for generation of FHG and SiHG through cascading optical nonlinearities.

Spectral translation of a tunable IR comb to create tunable combs in multiple visible regions requires phase matching across different wavelength regions. However, achieving intermodal phase matching across multiple wavelength windows is not easy and requires engineering of the fiber dispersion. To achieve wideband intermodal phase matching, we calculated the modal dispersion for fiber tapers of different diameters and found that tapers with waist diameters around 900 nm provide phase matching of the IR pump mode with higher-order modes at the SHG, THG, FHG, and SiHG wavelengths [see Fig. 2(a)]. Figure 1(b) plots the modal dispersion of the pump and higher-order modes around the second- and third-harmonic wavelengths for a taper with 900 nm waist diameter [see Fig. 2(a) for the modal dispersion at wavelengths near FHG and SiHG wavelengths]. While signals at the second- and third-harmonic wavelengths originate through intermodal phase matching of the optical mode at 1550 nm with the higher-order modes at the SHG and THG wavelengths, FHG and SiHG occur due to cascading of the nonlinearities, as shown in Fig. 1(c). In our work, FHG occurs due to four-wave mixing between the SHG and THG signals (see S2.C in the Supplemental Material [35] and Fig. 2), whereas SiHG results from the SHG of the THG signal [see Fig. 1(c)].

To clearly demonstrate the importance of dispersion engineering in intermodal phase matching and cascading of nonlinearities, we fabricated tapers T1 and T2 with diameters ∼900 nm and ∼1.7 μm, respectively, and losses 1.4 and 1.33 dB, respectively (see Sec. S3 in the Supplemental Material [35]). Figures 2(a) and 2(b) show the calculated modal dispersion n_{eff} as a function of wavelength, for tapers T1 and T2, respectively. The insets in Figs. 2(a) and 2(b) show the

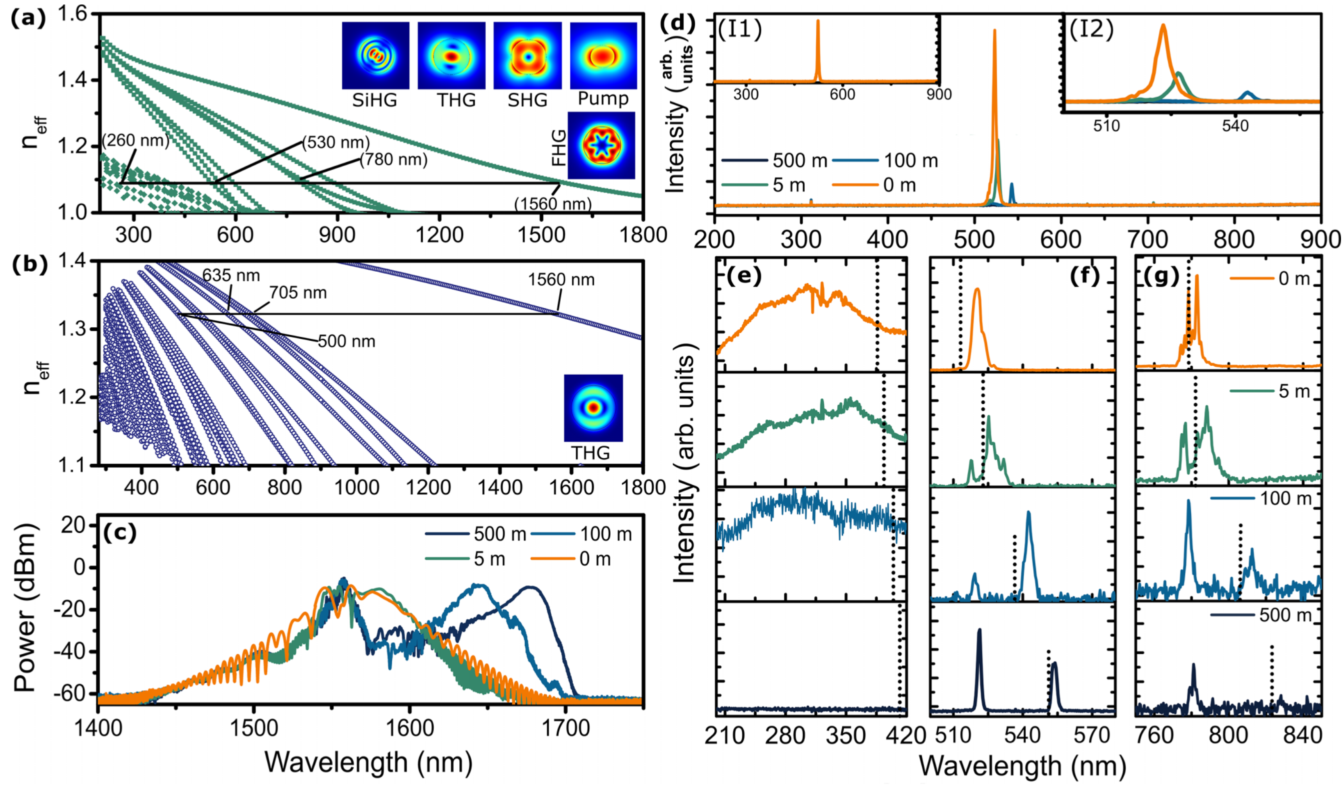

FIG. 2. Role of dispersion engineering in tunable harmonic generation through broadband phase matching: (a) Modal dispersion, effective refractive index n_{eff} as a function of wavelength, and images for phase-matched harmonic modes for taper T1 with a waist diameter of 900 nm. (b) Modal dispersion for taper T2 with a waist diameter of 1.7 μm, and the calculated phase-matched mode at the THG wavelength. (c) Optical spectra showing redshift of the input IR pulse spectrum after propagation through different lengths of SMF. (d) Spectra of the harmonics generated in a 1.7 μm taper. The spectra in (d) were obtained using an integration of 700 ms. Inset I1 is the spectra observed for 4 seconds of integration time, showing that even for longer integration times, only THG was observed in taper T2. Inset I2 shows the zoomed-in version of the THG peaks in T2. (e)–(g) Spectrum of the generated harmonics in a 900 nm taper. (e) SiHG and FHG, (f) THG, (g) SHG. The vertical dotted line in each panel shows the perfect phase-matching wavelength λ_s/N, where N is the order of the harmonic signal and λ_s is the wavelength of the redshifted IR soliton.

simulated mode profiles for the higher-order modes close to the harmonic wavelengths. From the modal dispersion plots, we note that taper T1 has higher-order modes near the SHG, THG, FHG, and SiHG wavelengths [see Fig. 2(a)], whereas, for taper T2, the higher-order mode is far from the SHG wavelength of 780 nm [see Fig. 2(b)]. We, therefore, expect only taper T1 to achieve tunable harmonic generation in multiple visible regions and excitation of only THG in taper T2.

To study the tunable harmonic generation in tapers T1 and T2, we propagate an input pulse of pulse energy 0.86 nJ and pulse width of 250 fs, which is obtained from an IR mode-locked fiber laser with a repetition rate of 82 MHz, through SMFs of different lengths. Figure 2(c) shows tuning of the IR pump spectra by more than 100 nm as the input pulse is propagated through different lengths of SMF. When the IR pulses shown in Fig. 2(c) are propagated through tapers T1 and T2, only THG was observed in taper T2 [see Fig. 2(d)], whereas, for taper T1, we achieve simultaneous generation of SHG, THG, FHG, and SiHG [see Figs. 2(e)–2(g)], as expected from our discussion above. In Fig. 2(d), THG for taper T2 was obtained using an integration time of 700 ms, whereas THG for taper T1 in Fig. 2(f) was observed using an integration time of 4 ms, which shows that T1 provides better phase matching for THG and thus higher efficiency compared to T2. Further, when the redshifted soliton from a 500-m-long SMF was launched into T1 and T2, which have similar losses, only T1 showed tuning of THG, even though much lower integration time was used to obtain THG for T1, and no THG was observed for T2. We did not observe any other harmonic in T2, even for an integration time of ∼10 s, whereas all four harmonics were observed in T1. Inset I1 of Fig. 2(d) shows the THG spectra for taper T2 with an integration time of 4 s. From the above discussion, it is evident that even though the same redshifted solitons were propagated through T1 and T2, only the taper that provides better intermodal phase matching was able to achieve efficient tunable harmonic generation across multiple visible regions, which shows that a SSFS-mediated tunable IR comb alone cannot achieve the simultaneous generation of a tunable comb across multiple visible regions unless we use a device with proper dispersion engineering.

While THG and SHG were obtained through direct translation of the IR pump mode to higher-order modes, SiHG and FHG were obtained through cascading of nonlinearities, as shown in Fig. 1. We achieve SiHG from the second-harmonic generation of the THG signal [13]. To understand the origin of the fourth-harmonic generation in T1, we looked at the detuning of the Nth harmonic from the perfectly phase-matched harmonic wavelength λ_s/N [37,38] [vertical dashed lines in

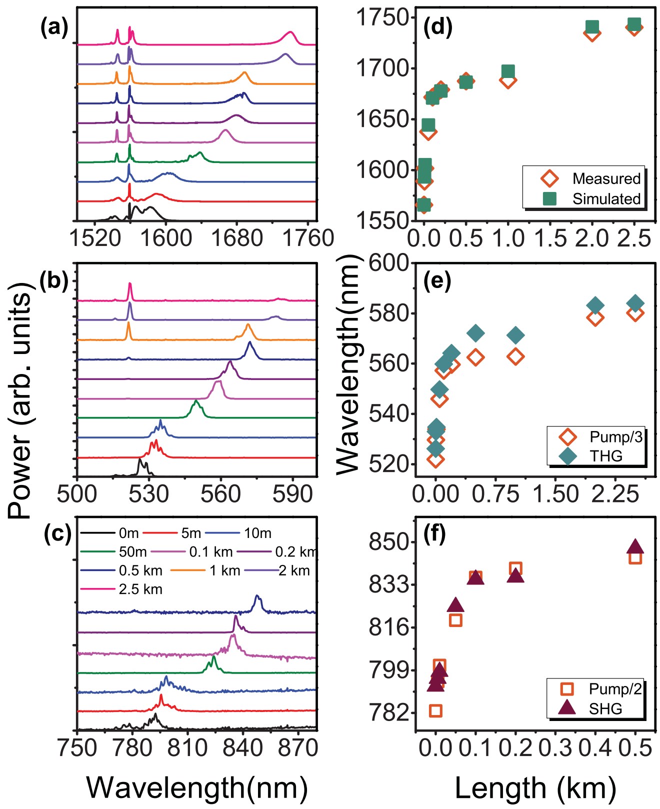

FIG. 3. Fiber-length dependence of the IR and visible spectra. (a) Evolution of the IR spectra with SMF length. (b), (c) Optical spectra of the THG and SHG signal. (d) Measured (diamonds) and theoretically estimated (green squares) IR pulse wavelength for different SMF lengths. (e) Comparison of the measured (filled diamonds) and estimated (open diamonds) THG wavelength. (f) Comparison of the measured (filled triangles) and estimated (open squares) SHG wavelength.

Figs. 2(e)–2(g)], when a soliton with a redshifted wavelength λ_s is launched into T1. From Figs. 2(f) and 2(g), we note that THG and SHG are redshifted with respect to $\lambda_s/3$ and $\lambda_s/2$, respectively, whereas FHG is blueshifted with respect to $\lambda_s/4$ [see dashed lines in Figs. 2(e)–2(g)]. Therefore, the fourth harmonic cannot result from the second harmonic of the SHG signal or sum frequency of SHG and pump, as both pathways will red detune FHG with respect to $\lambda_s/4$ (see Sec. S2.C, Eqs. (10)–(17), in the Supplemental Material [35]). The only pathway for which FHG is blue detuned with respect to perfectly phase-matched wavelength $\lambda_s/4$ is four-wave mixing (FWM), as explained in Sec. S2.C in the Supplemental Material [35]. Further, silica has much stronger $\chi^{(3)}$ nonlinearity than $\chi^{(2)}$, which arises due to the surface-induced nonlinearity in nanowires. The blue detuning of the FHG signal from $\lambda_s/4$ and occurrence of four-wave mixing due to $\chi^{(3)}$ nonlinearity, which is much stronger than $\chi^{(2)}$, therefore, makes FWM the favored pathway for FHG. Here, we present results for the tuning of combs with SMF length and input pump power only for tapers that achieve the simultaneous generation of SHG, THG, FHG, and SiHG.

Figure 3(a) shows the normalized SSFS spectra at the output of the SMFs of different lengths for an input IR pulse with 0.9 nJ energy and 293 fs full width at half maximum (FWHM) pulse width. From Fig. 3, we note that the wavelength of the IR pulse redshifts from 1560 to ∼1750 nm with an increase in SMF length [see Fig. 3(a)]. Propagation of the Raman-shifted pulses through a taper then results in the upconversion through THG and surface-nonlinearity-mediated SHG. Figures 3(b) and 3(c) show the normalized THG and SHG spectra, respectively, at the output of the taper for different SMF lengths before it. Since the SHG efficiency is smaller than the THG signal in the taper [13], we did not observe the SHG signal for long SMF lengths. We vary the integration time to obtain the THG and SHG spectra, in Figs. 3(b) and 3(c), for different SMF lengths before the taper.

Figure 3(d) plots the wavelength of the redshifted IR pulse (diamonds) along with the simulated soliton wavelength (squares), which is obtained by solving the generalized nonlinear Schrodinger equation (see Sec. S1, Eq. (3), in the Supplemental Material [35]), as a function of the SMF length. The rate of redshift of the IR pulse reduces for $L > 200$ m due to a decrease in the pump power with length and an increase in $|\beta_2|$ for the redshifted soliton [see Fig. 3(d)]. Figures 3(e) and 3(f) plot the wavelengths of the redshifted THG and SHG signals, respectively, demonstrating tuning of the THG wavelength from 520 to 580 nm and SHG signal from 780 to ∼850 nm. For longer SMF lengths, the power of the THG signal reduces significantly, as seen from Fig. 3(b). For SHG, no signals were observed for SMF lengths >500 m. To analyze the phase matching of the redshifted IR soliton wavelength ($\lambda_{IR}^{\text{Raman}}$) with the measured THG (filled diamond) and SHG (triangle) signals, we plot $\frac{\lambda_{IR}^{\text{Raman}}}{3}$ (diamond) and $\frac{\lambda_{IR}^{\text{Raman}}}{2}$ (squares) in Figs. 3(e) and 3(f) along with the measured THG and SHG wavelengths. The measured THG and SHG wavelengths show a good agreement with the estimated values of $\frac{\lambda_{IR}^{\text{Raman}}}{3}$ and $\frac{\lambda_{IR}^{\text{Raman}}}{2}$, respectively, which suggests that the nanowire provides a good phase matching of the pump mode with the higher-order modes at the harmonic frequency.

To study the pump-power-controlled Raman shift of the IR soliton frequency and the resulting harmonic signal frequency, we vary the pump power to the SMF using an attenuator, while keeping the length fixed at 100 m. Figure 4(a) plots the spectral evolution of the IR soliton as the pulse power is varied from 40 mW (0.5 nJ) to 68 mW (0.8 nJ). From Fig. 4(a), we note that the bandwidth of the IR soliton is larger at the Raman-shifted wavelength than at the pump wavelength. The SSFS transfers significant power (∼66%) from the input pump wavelength to the Raman-shifted wavelength. The harmonic signals are, therefore, generated mainly due to the Raman-shifted soliton. Figures 4(b) and 4(c) plot the measured THG and SHG spectra, respectively, at the output of a taper, which is connected to a 100-m-long SMF. The THG and SHG signal wavelength increases with an increase in the pump power, which confirms that the harmonic signals are generated due to the Raman-shifted soliton.

Figure 4(d) plots the wavelength of the IR soliton for different pump powers, showing a wavelength tuning from 1580 to 1640 nm. The solid line in Fig. 4(d) shows the theoretically calculated redshifted IR wavelength as a function of the pump power. The wavelengths of the measured THG and SHG spectra in Figs. 4(b), and 4(c) are plotted in Figs. 4(e)

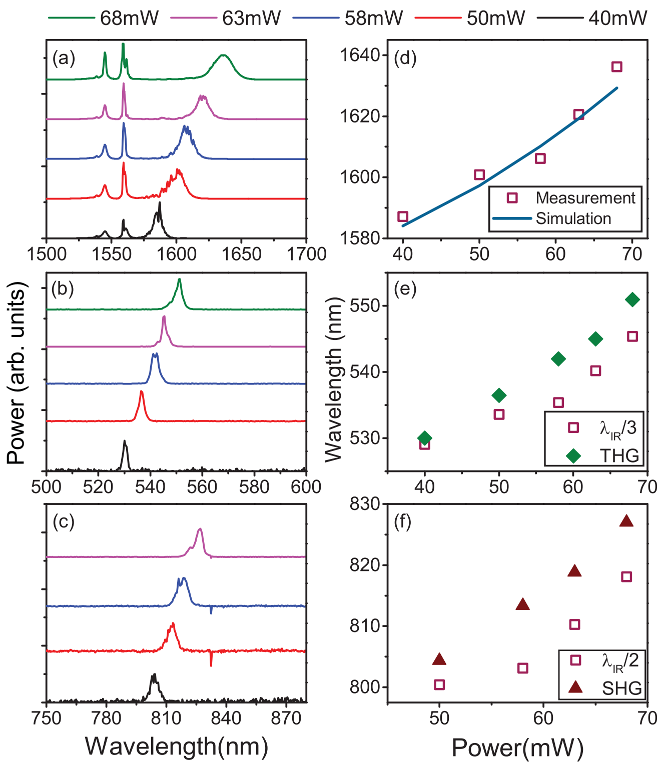

FIG. 4. Power-dependent redshift of IR pulse and harmonic frequencies. (a) Optical spectra of the IR pulse at the output of a 100-m-long SMF for different input pump powers. (b), (c) THG and SHG spectra at the output of the 100 m SMF + taper system. (d) Measured (squares) and theoretically estimated (solid) (see Eq. (2) in the Supplemental Material [35]) IR wavelength corresponding to (a). (e) Measured (diamond) and estimated (square) THG wavelength corresponding to (b). (f) Measured (triangle) and estimated (square) SHG wavelength corresponding to (c).

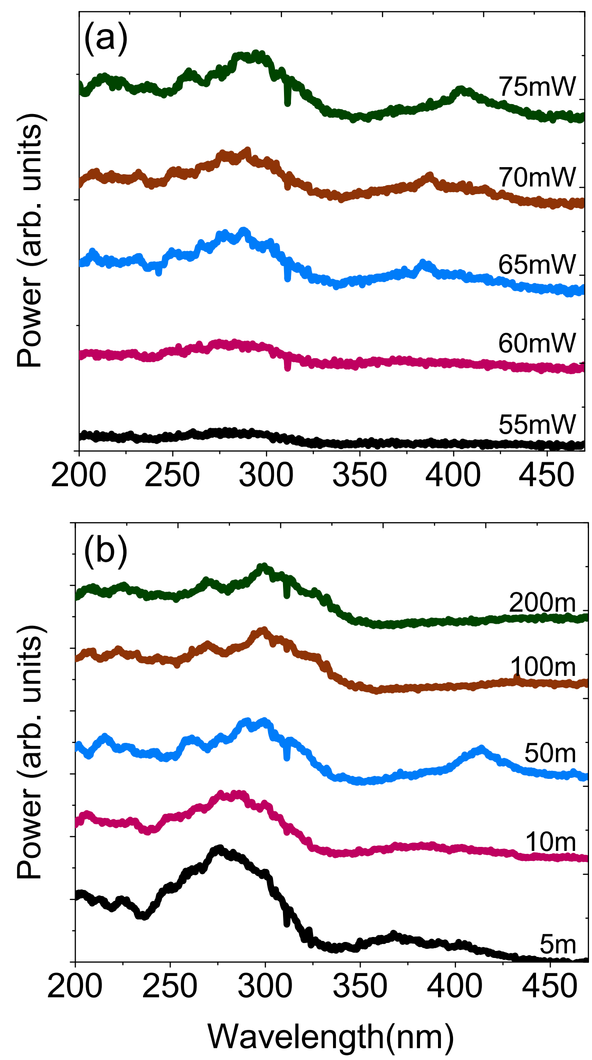

FIG. 5. Fourth- and sixth-harmonic generation (FHG, SiHG): (a) pump-power-dependent tuning of the FHG and SiHG using 50 m SMF before the taper; (b) tuning of the FHG and SiHG signals with variation in the SMF length.

and 4(f), respectively. The THG and SHG wavelengths follow a similar trend with the pump power as the IR pulse. In order to study the effect of the pump power on the phase matching of the THG and SHG signal mode with the pump mode, we plot $\frac{\lambda_{IR}^{\rm Raman}}{3}$ and $\frac{\lambda_{IR}^{\rm Raman}}{2}$ (open squares) in Figs. 4(e) and 4(f) along with the measured THG (diamond) and SHG (triangle) wavelengths. For a pump power of 40 mW, the wavelength of the measured THG signal is nearly the same as the THG wavelength estimated from the Raman-shifted soliton. This shows that a nearly perfect phase matching is achieved for low pump powers, and the nonlinearity-induced phase-mismatch effect is minimal. For higher pump powers, we attribute the deviation of the measured THG and SHG wavelength from that estimated using the Raman-shifted soliton to nonlinearity-induced phase shift (see Eqs. (4) and (5) in the Supplemental Material [35]) [13,37,38]. Increasing the pump power, therefore, not only increases the magnitude of the IR pulse redshift, but also allows control of the harmonic signal wavelength through the nonlinearity-induced phase mismatch. We can, therefore, control the harmonic frequency coarsely, using the SSFS, and finely, through the pump-power-dependent nonlinear phase shift. We confirm the translation of the IR comb to visible by measuring the RF spectrum for different Raman-induced shifts of the pump and the THG signal (see Fig. 5 of the Supplemental Material [35]).

We simultaneously achieve SHG, THG, FHG, and SiHG in a taper by varying the input pulse parameters. We attribute the SiHG to the second-harmonic generation of the THG signal [13]. FHG can arise due to multiple pathways based on $\chi^{(3)}$ nonlinearity such as four-wave mixing (FWM) between the two THG photons and one SHG photon or through sum-frequency generation (SFG) exploiting two pump photons and one SHG photon. From the discussion of Fig. 2 in Sec. S2.C in the Supplemental Material [35], we infer that FWM is responsible for FHG in our demonstration. Further analysis in Sec. S2.C, Eqs. (6)–(17), in the Supplemental Material [35] shows that the FWM-based FHG explains the experimental observations and FWM provides far more flexibility in achieving phase matching for FHG. We did not observe any fifth harmonic due to the strict conditions for achieving phase matching for it (see Sec. S2.D, Eqs. (18)–(22), in the Supplemental Material [35]). Figure 5(a) shows the power dependence of the SiHG signal around 280 nm and the FWM-generated FHG signal around 380 nm for a 50-m-long SMF before the taper. The pump-power-dependent redshift of the IR, THG, and SHG signals results in tuning of the SiHG and FHG for a fixed SMF length. For a fixed pump power, we study the dependence of the FHG and SiHG on the SMF length [Fig. 5(b)]. From Figs. 5(a) and 5(b), we note that the FHG and SiHG spectra are broad compared to THG and SHG. We attribute the broad FHG and SiHG spectra to the availability of many higher-order modes for phase matching around the wavelengths close to the fourth and sixth harmonics. This allows coupling of the pump spectra for FHG and SiHG to many higher-order modes at slightly different frequencies depending on the phase matching, which results in broadening of the FHG and SiHG spectra. As seen earlier, the increase in the SMF length tunes the harmonic frequency.

By combining the SSFS with dispersion engineering, it is therefore possible to translate the IR combs from compact MLLs to cover the entire wavelength region from 260 to 850 nm in a targeted manner to enable applications in photon-level spectroscopy and quantum interference. Unlike the supercontinuum generation, the SSFS-based creation and tuning of the visible comb concentrate the power only in the desired wavelength band of application, while providing access to any visible wavelength band. Further, MLL tuning and comb spectral translation using an all-fiber platform allows the transfer of combs to far-off locations. The use of tapers for tunable visible comb generation allows enhanced light-atom interaction through the trapping of atoms using a cw laser and probing them using a tunable comb.

We acknowledge the financial support of the Science and Engineering Research Board (SERB) of the Department of Science and Technology through Grant No. CRG/2019/000993.

R.P. proposed the experiments. A.M. fabricated the tapers and conducted the simulations. S.M. conducted the experiments. A.M. and R.P. analyzed the data. R.P. wrote the manuscript, with inputs from A.M. and S.M., and supervised the project.

The authors declare no competing interests.

[1] N. Picquéand T. W. Hänsch, Photon-level broadband spectroscopy and interferometry with two frequency combs, Proc. Natl. Acad. Sci. **117**, 26688 (2020).
[2] B. Xu, T. W. Hänsch, and N. Picqué, Near-ultraviolet dual-comb spectroscopy with photon-counting, in *CLEO: Science and Innovations* (Optica Publishing, San Jose, California United States, 2022), pp. SM1D–4.
[3] C. J. Sansonetti, C. E. Simien, J. D. Gillaspy, J. N. Tan, S. M. Brewer, R. C. Brown, S. Wu, and J. V. Porto, Absolute Transition Frequencies and Quantum Interference in a Frequency Comb Based Measurement of the ^{6,7}Li *D* Lines, Phys. Rev. Lett. **107**, 023001 (2011).
[4] C. Lee, S. T. Chu, B. E. Little, J. Bland-Hawthorn, and S. Leon-Saval, Portable frequency combs for optical frequency metrology, Opt. Express **20**, 16671 (2012).
[5] P. D. Reid and D. M. Ferrera, Compact visible frequency combs: The missing link in a vision of pervasive quantum timekeeping, Eng. Phys. Sci. Res. Council (2016).
[6] K. Nakamura, K. Kashiwagi, S. Okubo, and H. Inaba, Erbium-doped-fiber-based broad visible range frequency comb with a 30 GHz mode spacing for astronomical applications, arXiv:2110.03823.
[7] A. J. Benedick, G. Chang, J. R. Birge, L.-J. Chen, A. G. Glenday, C.-H. Li, D. F. Phillips, A. Szentgyorgyi, S. Korzennik, G. Furesz *et al.*, Visible wavelength astro-comb, Opt. Express **18**, 19175 (2010).
[8] A. G. Glenday, C.-H. Li, N. Langellier, G. Chang, L.-J. Chen, G. Furesz, A. A. Zibrov, F. Kärtner, D. F. Phillips, D. Sasselov *et al.*, Operation of a broadband visible-wavelength astro-comb with a high-resolution astrophysical spectrograph, Optica **2**, 250 (2015).
[9] S. Miller, K. Luke, Y. Okawachi, J. Cardenas, A. L. Gaeta, and M. Lipson, On-chip frequency comb generation at visible wavelengths via simultaneous second-and third-order optical nonlinearities, Opt. Express **22**, 26517 (2014).
[10] X. Guo, C.-L. Zou, H. Jung, Z. Gong, A. Bruch, L. Jiang, and H. X. Tang, Efficient Generation of a Near-visible Frequency Comb via Cherenkov-like Radiation from a Kerr Microcomb, Phys. Rev. Appl. **10**, 014012 (2018).
[11] J. Szabados, D. N. Puzyrev, Y. Minet, L. Reis, K. Buse, A. Villois, D. V. Skryabin, and I. Breunig, Frequency Comb Generation via Cascaded Second-Order Nonlinearities in Microresonators, Phys. Rev. Lett. **124**, 203902 (2020).
[12] M. L. Davenport, S. Liu, and J. E. Bowers, Integrated heterogeneous silicon/III-V mode-locked lasers, Photon. Res. **6**, 468 (2018).
[13] A. Mishra and R. Pant, Deep UV to NIR frequency combs via cascaded harmonic generation in a silica nanowire using nanojoule pulse energies, Optica **8**, 1210 (2021).
[14] F. M. Mitschke and L. F. Mollenauer, Discovery of the soliton self-frequency shift, Opt. Lett. **11**, 659 (1986).
[15] J. P. Gordon, Theory of the soliton self-frequency shift, Opt. Lett. **11**, 662 (1986).
[16] I. T. Sorokina, E. Sorokin, E. Wintner, A. Cassanho, and H. P. Jenssen, Raman induced pulse self-frequency shift in the sub-20 fs Kerr-lens mode-locked cr:lisgaf and cr:lisaf lasers, in *Advanced Solid State Lasers*, edited by F. X. Kärtner (Springer, 1998), p. TS8.
[17] J. Santhanam and G. P. Agrawal, Raman-induced spectral shifts in optical fibers: General theory based on the moment method, Opt. Commun. **222**, 413 (2003).
[18] J. H. Lee, J. van Howe, C. Xu, and X. Liu, Soliton self-frequency shift: Experimental demonstrations and applications, IEEE J. Sel. Top. Quantum Electron. **14**, 713 (2008).
[19] I. Cormack, D. Reid, W. Wadsworth, J. Knight, and P. S. J. Russell, Observation of soliton self-frequency shift in photonic crystal fibre, Electron. Lett. **38**, 167 (2002).
[20] R. Pant, A. C. Judge, E. C. Magi, B. T. Kuhlmey, M. de Sterke, and B. J. Eggleton, Characterization and optimization of

photonic crystal fibers for enhanced soliton self-frequency shift, J. Opt. Soc. Am. B **27**, 1894 (2010).

[21] A. C. Judge, S. A. Dekker, R. Pant, C. M. de Sterke, and B. J. Eggleton, Soliton self-frequency shift performance in As2S3 waveguides, Opt. Express **18**, 14960 (2010).

[22] D. V. Skryabin and A. V. Gorbach, Colloquium: Looking at a soliton through the prism of optical supercontinuum, Rev. Mod. Phys. **82**, 1287 (2010).

[23] S. A. Dekker, A. C. Judge, R. Pant, I. Gris-Sánchez, J. C. Knight, C. M. de Sterke, and B. J. Eggleton, Highly-efficient, octave spanning soliton self-frequency shift using a specialized photonic crystal fiber with low oh loss, Opt. Express **19**, 17766 (2011).

[24] H. Liu, J. Yao, and A. Puri, Second and third harmonic generation in BBO by femtosecond Ti: sapphire laser pulses, Opt. Commun. **109**, 139 (1994).

[25] D. J. Jones, S. A. Diddams, J. K. Ranka, A. Stentz, R. S. Windeler, J. L. Hall, and S. T. Cundiff, Carrier-envelope phase control of femtosecond mode-locked lasers and direct optical frequency synthesis, Science **288**, 635 (2000).

[26] G. Rodriguez, J. P. Roberts, and A. J. Taylor, Ultraviolet ultrafast pump–probe laser based on a Ti:sapphire laser system, Opt. Lett. **19**, 1146 (1994).

[27] T. Takaya, C. Su, K. de La Harpe, C. E. Crespo-Hernández, and B. Kohler, UV excitation of single DNA and RNA strands produces high yields of exciplex states between two stacked bases, Proc. Natl. Acad. Sci. **105**, 10285 (2008).

[28] E. E. Serebryannikov, A. B. Fedotov, A. M. Zheltikov, A. A. Ivanov, M. V. Alfimov, V. I. Beloglazov, N. B. Skibina, D. V. Skryabin, A. V. Yulin, and J. C. Knight, Third-harmonic generation by Raman-shifted solitons in a photonic-crystal fiber, J. Opt. Soc. Am. B **23**, 1975 (2006).

[29] J. Lægsgaard, Theory of surface second-harmonic generation in silica nanowires, J. Opt. Soc. Am. B **27**, 1317 (2010).

[30] G. P. Agrawal, *Nonlinear Fiber Optics*, 5th ed (Academic press, United States, 2012).

[31] F. Le Kien, V. Balykin, and K. Hakuta, Atom trap and waveguide using a two-color evanescent light field around a subwavelength-diameter optical fiber, Phys. Rev. A **70**, 063403 (2004).

[32] H. Xin, R. Xu, and B. Li, Optical trapping, driving and arrangement of particles using a tapered fibre probe, Sci. Rep. **2**, 818 (2012).

[33] E. Vetsch, D. Reitz, G. Sagué, R. Schmidt, S. Dawkins, and A. Rauschenbeutel, Optical Interface Created by Laser-Cooled Atoms Trapped in the Evanescent Field Surrounding an Optical Nanofiber, Phys. Rev. Lett. **104**, 203603 (2010).

[34] S. Spillane, G. Pati, K. Salit, M. Hall, P. Kumar, R. Beausoleil, and M. Shahriar, Observation of Nonlinear Optical Interactions of Ultralow Levels of Light in a Tapered Optical Nanofiber Embedded in a Hot Rubidium Vapor, Phys. Rev. Lett. **100**, 233602 (2008).

[35] See Supplemental Material at http://link.aps.org/supplemental/10.1103/PhysRevResearch.5.L022020 for contains analysis of the soliton self-frequency shift, harmonic generation, combs confirmation, and experimental details.

[36] Y. Hu, A. Tehranchi, S. Wabnitz, R. Kashyap, Z. Chen, and R. Morandotti, Improved Intrapulse Raman Scattering Control via Asymmetric Airy Pulses, Phys. Rev. Lett. **114**, 073901 (2015).

[37] A. Zheltikov, Multimode guided-wave non-3ω third-harmonic generation by ultrashort laser pulses, J. Opt. Soc. Am. B **22**, 2263 (2005).

[38] A. Zheltikov, Third-harmonic generation with no signal at 3ω, Phys. Rev. A **72**, 043812 (2005).